Evidence for Gas-phase Metal Deficiency in Massive Protocluster Galaxies at $z \sim 2.2$[*]

Zahra Sattari[1] , Bahram Mobasher[1], Nima Chartab[1] , Behnam Darvish[2] , Irene Shivaei[3,5] , Nick Scoville[1] , and David Sobral[4]

[1] Department of Physics and Astronomy, University of California, Riverside, 900 University Avenue, Riverside, CA 92521, USA; zahra.sattari@email.ucr.edu
[2] Cahill Center for Astrophysics, California Institute of Technology, 1216 East California Boulevard, Pasadena, CA 91125, USA
[3] Steward Observatory, University of Arizona, 933 North Cherry Avenue, Tucson, AZ 85721, USA
[4] Department of Physics, Lancaster University, Lancaster, LA1 4YB, UK

Abstract

We study the mass–metallicity relation for 19 members of a spectroscopically confirmed protocluster in the COSMOS field at $z = 2.2$ (CC2.2), and compare it with that of 24 similarly selected field galaxies at the same redshift. Both samples are Hα emitting sources, chosen from the HiZELS narrowband survey, with metallicities derived from the N2 $\left(\frac{[\mathrm{NII}] \lambda 6584}{\mathrm{H}\alpha} \right)$ line ratio. For the mass-matched samples of protocluster and field galaxies, we find that protocluster galaxies with $10^{9.9} M_{\odot} \leqslant M_* \leqslant 10^{10.9} M_{\odot}$ are metal deficient by 0.10 ± 0.04 dex (2.5σ significance) compared to their coeval field galaxies. This metal deficiency is absent for low-mass galaxies, $M_* < 10^{9.9} M_{\odot}$. Moreover, relying on both spectral energy distribution derived and Hα (corrected for dust extinction based on M_*) star formation rates (SFRs), we find no strong environmental dependence of the SFR–M_* relation; however, we are not able to rule out the existence of small dependence due to inherent uncertainties in both SFR estimators. The existence of 2.5σ significant metal deficiency for massive protocluster galaxies favors a model in which funneling of the primordial cold gas through filaments dilutes the metal content of protoclusters at high redshifts ($z \gtrsim 2$). At these redshifts, gas reservoirs in filaments are dense enough to cool down rapidly and fall into the potential well of the protocluster to lower the gas-phase metallicity of galaxies. Moreover, part of this metal deficiency could be originated from galaxy interactions that are more prevalent in dense environments.

Unified Astronomy Thesaurus concepts: Metallicity (1031); Galaxy evolution (594); Protoclusters (1297); High-redshift galaxy clusters (2007); Large-scale structure of the universe (902)

1. Introduction

In the standard Λ cold dark matter (ΛCDM) cosmological scenario, structures form from the growth of small fluctuations through gravitational instability. Dark matter structures grow by two main processes: by merging small halos to form the larger ones or by smooth accretion of dark matter from their immediate environment. Baryons fall into the potential well of these dark matter structures and feed galaxies within those structures with cold pristine gas, which allows them to form their stars. Galaxy clusters observed in the present universe are the largest virialized dark matter halos that are populated with massive and evolved galaxies (e.g., Dressler 1980; Balogh et al. 2004; Kauffmann et al. 2004; Peng et al. 2010). At high redshifts ($z \gtrsim 2$), most of these clusters have not yet had the time to virialize and consist of subhalos that will then merge and form the massive clusters present in the local universe. Direct observations of the progenitors of these clusters at high redshifts, known as protoclusters, provide useful information about the processes involved in the early stages of structure formation.

It is now well established that, at a given redshift, the interstellar medium (ISM) of massive galaxies is more metal-enriched than that of low-mass galaxies. This correlation, known as the mass–metallicity relation (hereafter MZR), is observed out to $z \sim 3.5$ (see review by Maiolino & Mannucci 2019, and references therein). The infall of cold gas from the intergalactic medium (IGM) provides the fuel for galaxies to form their stars, which are the factories responsible for metal production in galaxies. However, galaxies are not very efficient in forming stars as the cold gas accretes into their potential well. Behroozi et al. (2013a) found that the star formation efficiency of galaxies (the star formation rate (SFR) divided by the baryon accretion rate) can reach a maximum of $\sim 55\%$. Therefore, the extra primordial cold gas that could not convert to stars dilutes the metal content of the ISM. This mechanism can explain observations where, at a given stellar mass, galaxies with higher SFR have lower gas-phase metallicity (e.g., Lara-López et al. 2010; Mannucci et al. 2010; Stott et al. 2013; Sanders et al. 2018). More interestingly, many studies suggest that these two parameters, SFR and gas accretion rate, depend on the environment of galaxies even at high-redshift universe (Darvish et al. 2016; Kawinwanichakij et al. 2017; Chartab et al. 2020). Thus, comparing gas-phase metallicity of galaxies in extreme environments and high redshifts, such as protoclusters, with a similarly selected population of field galaxies at the same redshift can provide valuable insights about galaxy evolution processes and their environmental dependencies.

Although in the local universe most of the studies found evidence for environmental imprint on the MZR (e.g., Cooper et al. 2008; Ellison et al. 2009; Peng & Maiolino 2014; Sobral et al. 2015), environmental dependence of the MZR at high redshift is still controversial. Some studies found an enhancement in the gas-phase metallicity of galaxies in protoclusters compared to their field counterparts at $z \sim 2$ (Kulas et al. 2013;

---

[5] Hubble Fellow.

Shimakawa et al. 2015). However, there is observational evidence of metal deficiency in protocluster galaxies at $z \sim 2$ compared to their field counterparts, according to Valentino et al. (2015). Moreover, Chartab et al. (2021) studied the relation between the local density of MOSFIRE Deep Evolution Field (MOSDEF; Kriek et al. 2015) galaxies and their gas-phase metallicities and found that galaxies in overdensities have ~ 0.07 dex lower metallicity than the field galaxies at $z \sim 2.3$. On the other hand, Kacprzak et al. (2015) and Alcorn et al. (2019) found no significant environmental dependence on the MZR of galaxies at $z \sim 2$.

In this paper, we study the MZR for galaxy members of the recently confirmed protocluster, CC2.2, in the Cosmic Evolution Survey (COSMOS; Scoville et al. 2007) at $z \sim 2.2$ (Darvish et al. 2020). We then compare this relation with a control sample of similarly selected field galaxies. Both protocluster and field samples are $H\alpha$ emitting sources, selected from the narrowband High-Z Emission Line Survey (HiZELS; Geach et al. 2012; Sobral et al. 2013, 2014). The paper is organized as follows: In Section 2, we describe the Keck I/MOSFIRE observations and data reduction procedure followed by stellar mass measurements and sample selection. We then explain the stacking process and measurements of gas-phase metallicities in Section 3. In Section 4, we construct the MZR for both protocluster and field samples and compare them to deduce the role of the environment in MZR at $z \sim 2.2$. We discuss our results in Section 5.

Throughout this paper, we assume a flat ΛCDM cosmology with $H_0 = 70 \, \text{km s}^{-1} \, \text{Mpc}^{-1}$, $\Omega_{m_0} = 0.3$, and $\Omega_{\Lambda_0} = 0.7$. All the physical parameters are measured assuming a Chabrier (2003) initial mass function (IMF).

2. Data

2.1. MOSFIRE Observation

In this paper, we use near-IR spectroscopy of galaxies in a recently confirmed protocluster, CC2.2, at $z \sim 2.2$ (Darvish et al. 2020), in the COSMOS field (Scoville et al. 2007). The spectroscopic observations were conducted with Keck I/ MOSFIRE NIR multi-object spectrograph (McLean et al. 2012) in 2018 December and 2019 January in both the K ($\sim 1.92–2.40 \, \mu$m) and H ($\sim 1.47–1.81 \, \mu$m) bands, leading to 35 confirmed members. The primary spectroscopic sample comprises the narrowband $H\alpha$ emitting candidates from the HiZELS survey (Geach et al. 2012; Sobral et al. 2013, 2014). For a full description of the protocluster identification and observation, we refer readers to Darvish et al. (2020).

As a control sample, we use Keck I/MOSFIRE spectroscopic observations of 24 field galaxies in the redshift range $2.22 \leqslant z \leqslant 2.24$, located in less-crowded regions of the COSMOS (16 galaxies) and the Ultra Deep Survey (UDS) (8 galaxies) fields. All these field galaxies were observed over the observing programs during 2018–2019 (PI: N. Z. Scoville) in the K band (a few in the H band as well) and are selected similarly from the HiZELS survey to avoid any biases introduced by sample selection.

The observations were performed the same way for both field and protocluster galaxies, minimizing any source of bias. All the observing nights were conducted under clear conditions with the average seeing of $0.5''$, and a typical exposure time of ~ 90 minutes per mask.

2.2. Data Reduction

The acquired data were reduced using the MOSFIRE data reduction pipeline (DRP).[6] The outputs of the DRP are rectified, sky-subtracted, and wavelength-calibrated 2D spectra and their associated uncertainties. We then extract optimally weighted 1D spectra and their errors using the optimal extraction algorithm (Horne 1986). We weight the flux of each pixel by the inverse of the flux variance and the spatial extent of the 2D spectrum in an optimized window, and then sum the weighted fluxes along the wavelength axis. The size of the optimized window is determined such that the bright features with the highest signal-to-noise ratio (S/N) in the 2D spectrum are surrounded by the window. The weighted summation within the optimized window produces 1D spectra of the sources along with their errors. Figure 1 shows an example of the 2D and optimally extracted 1D spectra for a field galaxy and a protocluster member.

We fit a triple Gaussian function to the reduced 1D spectra to extract [N ii]λ6548, $H\alpha$, and [N ii]λ6584 emission line fluxes. We require a constant value for the continuum and the same width for all three emission lines. The line fluxes are the integration of the best-fit Gaussian function to the 1D spectra. For the error calculation, we perturb the 1D spectra 1000 times and remeasure the line fluxes. The standard deviation of these 1000 measurements is assigned as the uncertainty in line fluxes. The redshifts of the sources are measured based on the peak of $H\alpha$ emission lines with S/N $\geqslant 3$.

2.3. Stellar Masses and SFRs

We estimate the stellar masses (M_*) and SFRs of galaxies by fitting synthetic spectral energy distributions (SEDs) to their available photometric data (COSMOS: Laigle et al. 2016; UDS: Mehta et al. 2018). To perform the SED fitting, we utilize Bayesian Analysis of Galaxies for Physical Inference and Parameter EStimation (Bagpipes) code (Carnall et al. 2018), which uses the 2016 version of a library of Bruzual & Charlot (2003) synthetic spectra. We fix the redshifts of galaxies to their spectroscopic values, considering delayed exponentially declining star formation history, te$^{-t/\tau}$. A range of 0.3–10 Gyr with a uniform prior is assumed for the star formation e-folding timescale (τ). The nebular emission models that are constructed based on the methodology of Byler et al. (2017) are added to the SEDs. Also, a metallicity range $0 < Z/Z_\odot < 2.5$ with a logarithmic prior and a Calzetti et al. (2000) extinction law are adopted.

The SFRs of the galaxies are also estimated using their $H\alpha$ emission line fluxes taken from the HiZELS survey (Sobral et al. 2013). Since the H-band data are not available for most of the sample, following Sobral et al. (2012) and Koyama et al. (2013), we utilize the Garn & Best (2010) calibration to correct the $H\alpha$ luminosity for the dust extinction based on the stellar masses of the galaxies. We then convert the dust-corrected $H\alpha$ luminosity to SFR using the calibration from Kennicutt (1998): $\text{SFR}(M_\odot yr^{-1}) = 7.9 \times 10^{-42} L_{H\alpha}(erg \, s^{-1})$. One should note that the SFR derived from this method is highly uncertain due to the existence of a large scatter in dust attenuation calibration based on the stellar mass.

---

[6] https://github.com/Keck-DataReductionPipelines/MosfireDRP
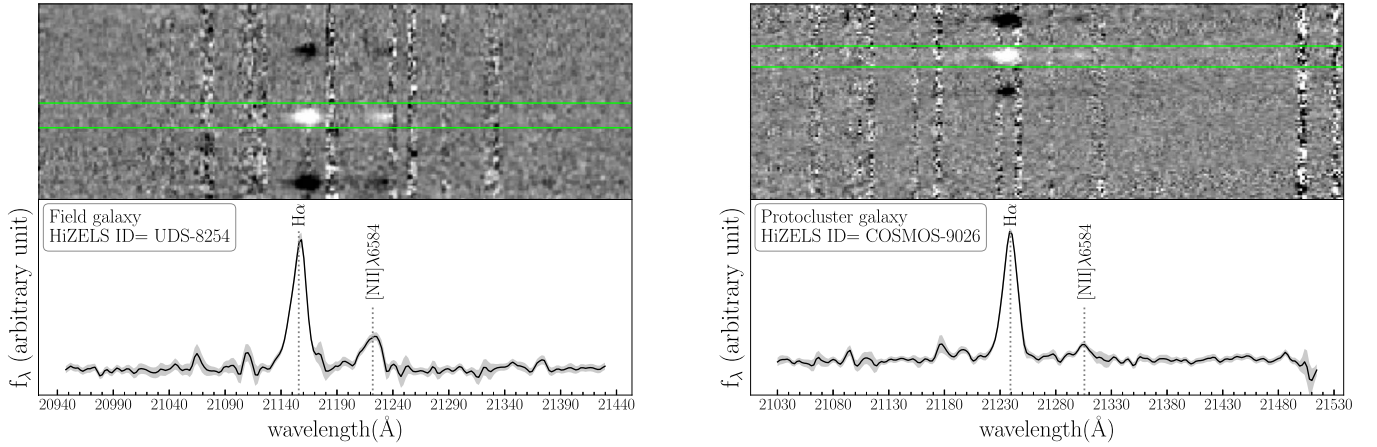
Figure 1. The 2D and corresponding optimally extracted 1D spectra for two galaxies selected from our sample. Left: example of a field galaxy. This galaxy is at $z = 2.223$ and has a stellar mass $10^{10.05} M_{\odot}$. Right: a galaxy member of the protocluster at $z = 2.235$. The stellar mass of this galaxy is $10^{9.96} M_{\odot}$. In both spectra, Hα and [N ii]λ6584 emission lines are evident.

2.4. Sample Selection

We select galaxies with significant detection in Hα emission lines (S/N $\geqslant$ 3). We exclude galaxies with $M_* < 10^{9.5} M_{\odot}$ to construct a mass complete sample. We also remove potential mergers by visual inspection of their spectra and images, as well as the active galactic nuclei (AGNs). The AGNs are identified through their broad emission lines, X-ray flags included in the UDS and COSMOS catalogs, or IR emissions (Donley et al. 2012). Moreover, optical AGNs are excluded by requiring $\log\left(\frac{[NII]\lambda6584}{H\alpha}\right) < -0.3$ (Coil et al. 2015). These criteria result in 19 protocluster members at $z = 2.23$ and 24 field galaxies at the same redshift, spanning a narrow redshift range $2.22 \leqslant z \leqslant 2.24$.

3. Composite Spectra

3.1. Stacking Analysis

We measure the gas-phase metallicity of galaxies, using the N2 $\left(\frac{[NII]\lambda6584}{H\alpha}\right)$ line ratio. Due to the prevalence of [N ii]λ6584 undetected galaxies in our low-mass sample (S/N < 3), we use a stacking technique. To stack the spectra, we divide the sample into three stellar mass bins, with an equal number of objects in each bin, for both the protocluster and field galaxies. We provide the range of stellar mass bins and the number of galaxies residing in each bin for the field and protocluster samples in Table 1. We then shift the spectra of galaxies to their rest frame and normalize them by the total Hα luminosity. In each mass bin, we bin the normalized spectrum with a resolution of 0.5 Å. The stacked spectrum is calculated as the weighted average of the spectra in each 0.5 Å bin:

$$\tilde{f}(\lambda)^{\text{stacked}} = \frac{\sum_i \frac{\tilde{f}_i(\lambda)}{\sigma_i^2}}{\sum_i \frac{1}{\sigma_i^2}}, \quad (1)$$

where $\tilde{f}_i(\lambda)$ is the flux density of each normalized spectrum, σ_i is its corresponding standard deviation, and $\tilde{f}(\lambda)^{\text{stacked}}$ is the composite spectrum with the uncertainty of $\sqrt{1/\left(\sum_i \frac{1}{\sigma_i^2}\right)}$ in each mass bin. The protocluster and field galaxies are also bootstrap resampled 100 times to take into account the sample variance. To perform the bootstrap resampling, we draw a random

Table 1
The Stellar Mass Range of Each Mass Bin in the Stacking Process

| Sample	$\log \frac{M_*}{M_{\odot}}$	Number of Galaxies
Field	[9.5, 9.7)	8
	[9.7, 10)	8
	[10, 10.8]	8
Protocluster	[9.5, 9.8)	7
	[9.8, 10.5)	6
	[10.5, 11.2]	6

sample of galaxies from the original sample considering replacement. The replacement allows us to have a random sample that may include some duplicate members from the original sample, or may not contain some of the galaxies from the initial sample. This process is repeated 100 times, and each time we end up having new stacked spectra. The sample variance is calculated using the standard deviation of these 100 trials.

3.2. Metallicities

Since only a few field galaxies are observed in the *H* band (~10% of the field galaxies), we utilize rest-frame optical emission line in the observed *K* band to measure the gas-phase metallicities. This is done by measuring the best-fit [NII]λ6584 and Hα emission line intensities and estimating the gas-phase metallicity using the N2 $\left(\frac{[NII]\lambda6584}{H\alpha}\right)$ line ratio.

To measure the line fluxes and their uncertainties for the stacked spectra, we use the same methodology described in Section 2.2 for the individual spectra. Since the stacked spectra are normalized by the Hα luminosity, the area underneath the [NII]λ6584 line in the stacked spectra corresponds to $\left\langle \frac{[NII]\lambda6584}{H\alpha} \right\rangle$.

In order to measure the gas-phase oxygen abundance $(12 + \log(O/H))$ of galaxies, we employ the empirical calibration from Pettini & Pagel (2004), which is based on electron temperature measurements in the local H ii regions, and is given by $8.9 + 0.57 \log(N2)$.
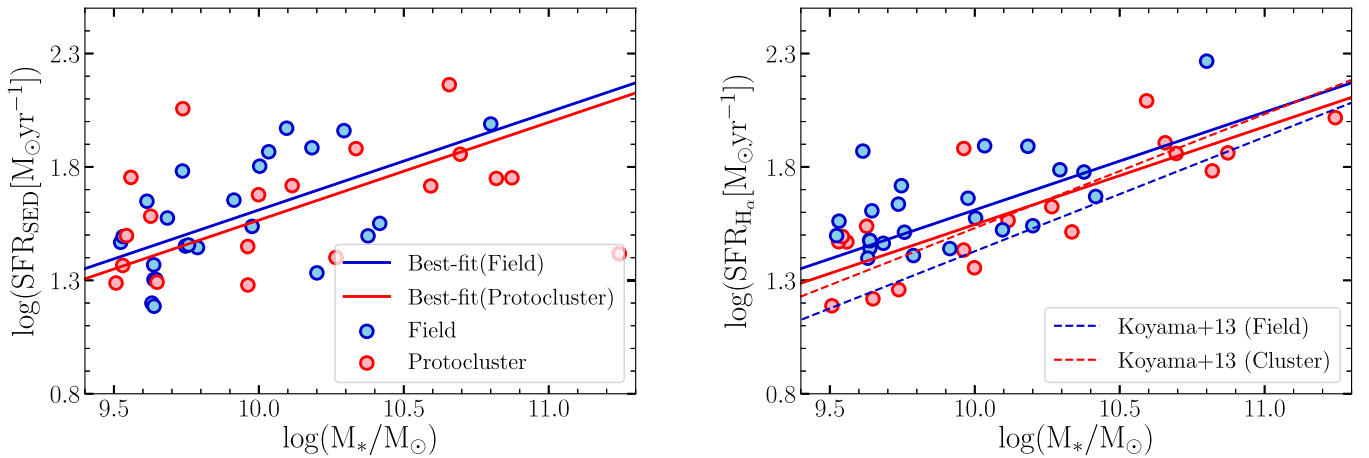
Figure 2. SFR of the field (blue circles) and protocluster (red circles) galaxies as a function of their stellar masses. Left: the SFRs are calculated from SED fitting. Right: the SFRs are determined using the Hα luminosity of galaxies corrected for the dust extinction based on their stellar masses. The solid lines in each panel show the best fit to the data points. The slope of the protocluster best-fit line (solid red lines) is fixed at the slope of the best-fit line for field galaxies (solid blue lines). The dashed blue (red) line shows the best fit for the field (cluster) galaxies from Koyama et al. (2013).

4. Results

4.1. SFR–M_* Relation

Different studies have shown that the fundamental metallicity relation (FMR) exists for galaxies at $z \sim 2$ (Mannucci et al. 2010; Sanders et al. 2018). According to this relation, at a given stellar mass, galaxies that have a higher SFR tend to have lower gas-phase metallicities. Thus, before studying the environmental dependence of the MZR in our sample, to investigate any possible dependence between the environment of the galaxies and their SFRs we show the relation between the SFR of the field and protocluster galaxies and their stellar masses in Figure 2. The SFR in the left panel is calculated from SED fitting, while the right panel shows the Hα SFRs (corrected for extinction as mentioned in Section 2.3) as a function of stellar mass.

An important issue in the SFR estimation using these two methods is that there are large uncertainties in both measurements. This will not allow us to rule out any small environmental dependence of the main sequence, if it exists. For a better comparison, we also add the best-fit line from Koyama et al. (2013) in the right panel of Figure 2. Our result is in agreement with theirs, showing no significant environmental dependence of the main-sequence galaxies for our star-forming sample.

4.2. Mass–Metallicity Relation

In this section, we study the MZR for the field and protocluster samples to investigate the role of the environment in the gas-phase metallicity of galaxies at fixed M_*. As discussed in Section 3.1, we divide the sample into three stellar mass bins with equal number of galaxies in each bin. Figure 3 shows the MZR for the stacked spectra and individual galaxies. The metallicities of the stacked spectra in three stellar mass bins are shown in blue (red) squares for field (protocluster) galaxies. The stellar mass uncertainty in the stacked data points shows 1σ scatter in each bin.

As shown in Figure 3, in the stellar mass range $10^{9.7} M_\odot \lesssim M_* \lesssim 10^{10.5} M_\odot$, the average protocluster galaxies have a relatively lower metallicity than the average field galaxies by ~ 0.1 dex. However, the gas-phase metallicity of low-mass galaxies, $M_* < 10^{9.7} M_\odot$, does not significantly

depend on the environment. Moreover, in the massive end of the MZR ($M_* > 10^{10.5} M_\odot$), due to the small number of field galaxies, we cannot draw robust conclusions on the MZR variation between the field and protocluster galaxies. In the following section, we match the stellar mass distributions of protocluster and field samples to properly isolate the effect of stellar mass from galaxy environment.

4.3. The Mass-matched Samples

It is known that protoclusters often host more massive galaxies compared to the field. Therefore, to have a reliable comparison between the metallicity of protocluster and field galaxies at fixed stellar mass, the two samples should have similar stellar mass distributions. Otherwise, any change in the MZR may be attributed to the differences in stellar mass distributions.

The left panel in Figure 4 shows the stellar mass distribution for the field and protocluster galaxies. It is clear that, for protocluster galaxies in the massive end of the distribution, there is no analog of the field galaxy, resulting in a biased comparison between field and protocluster samples. We resolve this by constructing the mass-matched samples. Similar to Chartab et al. (2021), we match the stellar mass distributions of field and protocluster galaxies with the resolution of $\log(M_*/M_\odot) = 0.1$ dex, which is the typical stellar mass uncertainty computed in Section 2.3. As a result of mass-matched distributions, we have the same number of protocluster and field galaxies in each stellar mass bin of $\log(M_*/M_\odot) = 0.1$ (green hatched region in the left panel of Figure 4).

However, there is not a unique way to subsample data and construct mass-matched samples. For instance, four protocluster galaxies are in the mass range $10^{9.5} M_\odot \leqslant M_* \leqslant 10^{9.6} M_\odot$, but just two field galaxies are in this range of stellar mass. Thus, to take into account all the galaxies that reside in each mass-matched region, we randomly subsample galaxies 500 times and each time we construct the stacked spectra and perturb them based on their uncertainties. The stacking process is the same as described in Section 3.1, where we consider both measurement errors and sample variance. The average and standard deviations of 500 trials correspond to the composite spectrum and its error,
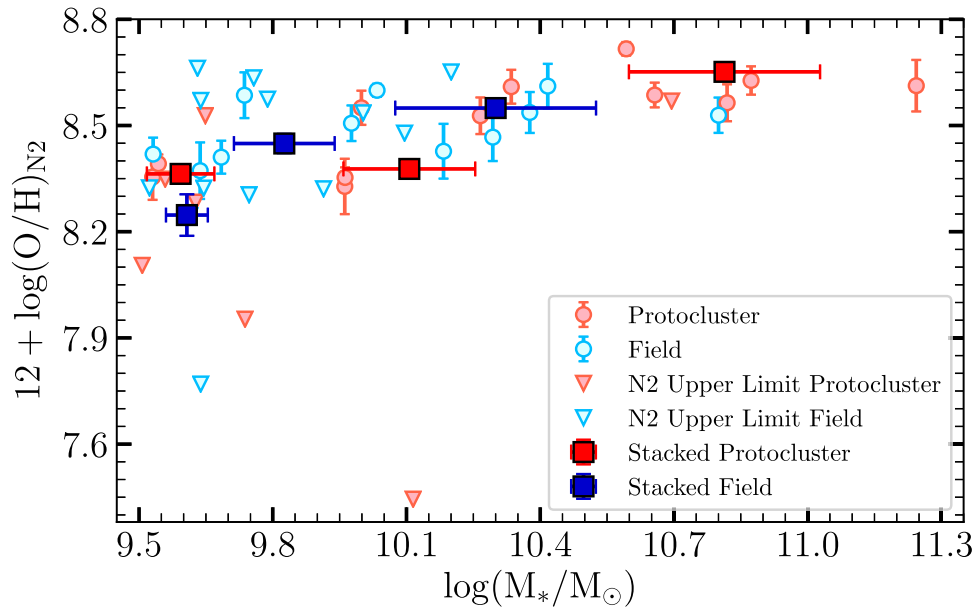
Figure 3. MZR for the field (blue circles) and protocluster (red circles) galaxies at $z \sim 2.2$, without controlling for the stellar mass distribution (mass matching). The 1σ upper limits for galaxies with undetected [N ii]$\lambda6584$ line are shown with inverted triangles. The solid blue (red) squares indicate the metallicity measurements for stacked spectra of field (protocluster) galaxies in three bins of stellar mass. The error bars are smaller than the square symbols if not shown. Also, the horizontal error bars in the stacked data show the 1σ scatter in the stellar mass of each bin.

respectively. The right panels in Figure 4 show the composite spectra for the mass-matched sample of protocluster and the field galaxies in two stellar mass bins $10^{9.5} M_\odot \leqslant M_* < 10^{9.9} M_\odot$ and $10^{9.9} M_\odot \leqslant M_* \leqslant 10^{10.9} M_\odot$.

We report the gas-phase metallicities of the field and protocluster galaxies for the mass-matched samples in Table 2. Red (blue) squares in Figure 5 (top panel) show the MZR for the stacked protocluster (field) sample in two stellar mass bins $10^{9.5} M_\odot \leqslant M_* < 10^{9.9} M_\odot$ and $10^{9.9} M_\odot \leqslant M_* \leqslant 10^{10.9} M_\odot$. The metallicity estimates for all the galaxies in the mass-matched samples are also included in the figure. At $z \sim 2.2$, the protocluster galaxies in the massive end of the MZR are metal deficient by 0.10 ± 0.04 (2.5σ significance) dex compared to those residing in the field. However, this deficiency is not significant ($<1\sigma$) in the lower-mass bin (0.03 ± 0.06 dex), possibly due to the prevalence of nondetections and/or small sample size.

4.4. Comparison with Literature

To compare our results with those in the literature, we show the offset between the average gas-phase metallicity of the protocluster (galaxies in overdense regions) and the field galaxies from different studies (including the present work) as a function of stellar mass in Figure 5 (bottom panel).

We emphasize that gas-phase metallicity is calibrated locally and its absolute value at high redshift could be uncertain (Steidel et al. 2014; Shapley et al. 2019). However, when we study relative metallicity and estimate the difference of metallicities between field and protocluster galaxies, the calibration effect is not a concern.

Moreover, consideration of selection biases is essential in measuring the MZR (Stott et al. 2013). Different selection criteria for protocluster and field samples result in an unreliable comparison between their respective metallicities. As both protocluster and field samples in the present work are Hα

selected, the metallicity offset does not suffer from such selection biases.

Kulas et al. (2013) studied the MZR of a protocluster sample at $z = 2.3$ and compared it with field galaxies at the same redshift. Both samples are selected based on their rest-frame UV emission. The gas-phase metallicity of their sources is calculated using N2 indicator. In the lower stellar mass bin ($M_* \sim 10^{10} M_\odot$), they found an offset of 0.15 dex between the metallicity of protocluster and field galaxies, i.e., their field sample is more metal deficient than the protocluster. Our result is in contrast with their findings, possibly due to the fact that they did not employ mass-matched samples.

Also, in the stellar mass range covered in this paper, Shimakawa et al. (2015) found metallicity enhancement (~ 0.15 dex) for two protoclusters at $z = 2.2$ and $z = 2.5$ compared to the field sample of Erb et al. (2006) at $z = 2.2$. A part of this enhancement can be caused by different selection criteria they used for protocluster and field samples (Their protoclusters are narrowband selected, but the field sample from Erb et al. 2006 is UV selected). Comparing our field sample with the UV selected sample of Erb et al. (2006), we notice that in the low-mass end of the MZR, the narrowband selected sample has systematically higher metallicity compared to the UV selected sample. Thus, the disagreement between the present work and Shimakawa et al. (2015) can be originated from selection biases.

Kacprzak et al. (2015) found no significant difference between the MZR of a protocluster at $z = 2$ and a field sample at the same redshift. On the other hand, Valentino et al. (2015) found that a protocluster sample at $z \sim 2$ with $M_* \sim 10^{10.5} M_\odot$ is 0.25 dex metal deficient compared to field galaxies at the same redshift. Their results are in qualitative agreement with the results in this study; however, we find ~ 0.1 dex metal deficiency for protocluster galaxies compared to the field sample in the massive end of the MZR at $z \sim 2.2$. Moreover, Chartab et al. (2021) recently studied the environmental dependence of the MZR for a sample of H-band selected
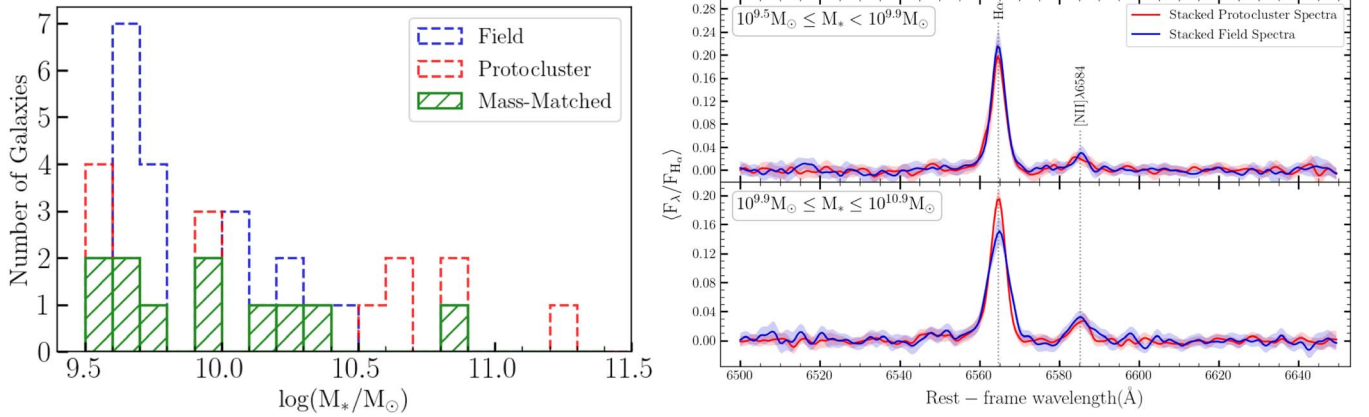
Figure 4. Left: the stellar mass distributions for the field (blue) and protocluster (red) galaxies. The green hatched region shows the matched stellar mass distributions of protocluster and field galaxies. Right: composite spectra for the mass-matched samples in two bins of stellar mass ($10^{9.5}\,M_\odot \leqslant M_* < 10^{9.9}\,M_\odot$ and $10^{9.9}\,M_\odot \leqslant M_* \leqslant 10^{10.9}\,M_\odot$). The stacked spectra of protocluster galaxies are shown in red, and the stacked spectra of field galaxies are shown in blue.

Table 2
Gas-phase Metallicities of the Stacked Spectra for the Mass-matched Samples

Environment	$\log \frac{M_*}{M_\odot}$	$\left\langle \log \frac{M_*}{M_\odot} \right\rangle$	$\langle 12 + \log(\mathrm{O/H}) \rangle$
Field	[9.5, 9.9]	9.62 ± 0.04	8.38 ± 0.04
	[9.9, 10.9]	10.25 ± 0.12	8.50 ± 0.03
Protocluster	[9.5, 9.9]	9.62 ± 0.03	8.35 ± 0.05
	[9.9, 10.9]	10.25 ± 0.12	8.40 ± 0.03

Note. The second and third columns show stellar mass ranges and the mean value of mass in each range, respectively.

galaxies in the MOSDEF survey at $1.37 \leqslant z \leqslant 2.61$. For a mass-matched sample in the redshift range $2.09 \leqslant z \leqslant 2.61$, they found ~ 0.07 dex metal deficiency for galaxies in overdense regions compared to field galaxies. As shown in the bottom panel of Figure 5, our results are in agreement with their findings. Additionally, they found that this metal deficiency increases by the stellar mass, which is also seen in our result in Figure 5 (top panel).

5. Summary and Discussion

In this paper, we studied the mass–metallicity relation for 19 galaxies in a spectroscopically confirmed protocluster at $z \sim 2.2$ in the COSMOS field and compared it with the MZR of a field sample with 24 galaxies at the same redshift. We used the $\frac{[\mathrm{NII}]\,\lambda 6584}{\mathrm{H}\alpha}$ ratio to measure the gas-phase metallicity of these galaxies. After matching the stellar mass distributions of field and protocluster samples, we found that the protocluster galaxies with $10^{9.9}\,M_\odot \leqslant M_* \leqslant 10^{10.9}\,M_\odot$ are 0.10 ± 0.04 dex (2.5σ significance) metal deficient in comparison to field galaxies at the same redshift. However, this metal deficiency is not significant for low-mass galaxies.

Darvish et al. (2020) predicted that this protocluster will grow to a Coma-type cluster with $\sim 9 \times 10^{14}\,M_\odot$ at $z = 0$. Dekel & Birnboim (2006) found that at $z \lesssim 2$, halos with $M_{\mathrm{halo}} \gtrsim 10^{12}\,M_\odot$ will be dominated with hot-mode accretion. However, as we go to higher redshifts, cold streams can penetrate massive halos from filaments hosting dense pristine gas (Kereš et al. 2005). Based on halo mass evolution trajectories of Behroozi et al. (2013b), we estimate that the progenitor of this protocluster at $z \gtrsim 2.5$ has $M_{\mathrm{halo}} \lesssim 10^{13.5}\,M_\odot$, where the protocluster is in a phase that hosts cold streams in

hot media (Dekel & Birnboim 2006). Therefore, the observed protocluster at $z = 2.2$ was experiencing cold streams until ~ 0.5 Gyr ago ($z \gtrsim 2.5$), which dilutes the gas-phase metallicity of galaxies residing in the protocluster. After the termination of cold streams, the protocluster galaxies continue to process their gas reservoirs until their star formation fully shuts down. However, 0.5 Gyr is a short time for the protocluster galaxies to significantly enrich their ISM metal content due to star formation. As a result, we are still witnessing metal deficiency for the members of this protocluster at $z = 2.2$ compared to field galaxies. We also expect that the SFRs of the protocluster galaxies increase due to a higher fraction of cold gas, but we are not able to confirm this effect, possibly due to the small sample size and inherent uncertainties in SED-derived and Hα (mass-dependent extinction corrected) SFRs, which prevent us from detecting weak environmental dependence of SFR at a given M_*. Future H-band spectroscopies of our sample can properly constrain the environmental dependence of SFR given the dust-corrected Hα luminosities, where the attenuation is derived from Balmer decrements.

In addition, the prevalence of minor/major mergers in dense environments at high redshifts (Hine et al. 2016; Watson et al. 2019) can explain a part of the metal deficiency observed in the present work. Although we exclude potential ongoing mergers in our sample, our protocluster galaxies could be descendants of recently merged galaxies at higher redshifts. Minor and major mergers could provide a higher fraction of cold pristine gas for galaxies, increasing their SFR and lowering their metallicities (Horstman et al. 2021).

Moreover, the stellar mass dependence of metal deficiency (i.e., the absence of significant metal deficiency for low-mass galaxies) can be explained by (1) massive galaxies located in deeper potential wells, being fed by metal-poor cold streams from the cosmic web (Dekel et al. 2009), and (2) Scaling of the merger fraction with the stellar mass of the galaxies. Duncan et al. (2019) showed that the major merger fraction for massive galaxies ($M_* > 10^{10.3}\,M_\odot$) is 3 times higher than low-mass galaxies with $10^{9.7}\,M_\odot < M_* < 10^{10.3}\,M_\odot$ at $z = 2$.

We speculate that the metal content of the protocluster members will rapidly increase at lower redshift as all the remaining cold gas reservoirs will be processed through star formation activity. In addition, the IGM gas within the protocluster will be enriched due to strong outflows, which will then reaccrete into galaxies and enhance their gas-phase
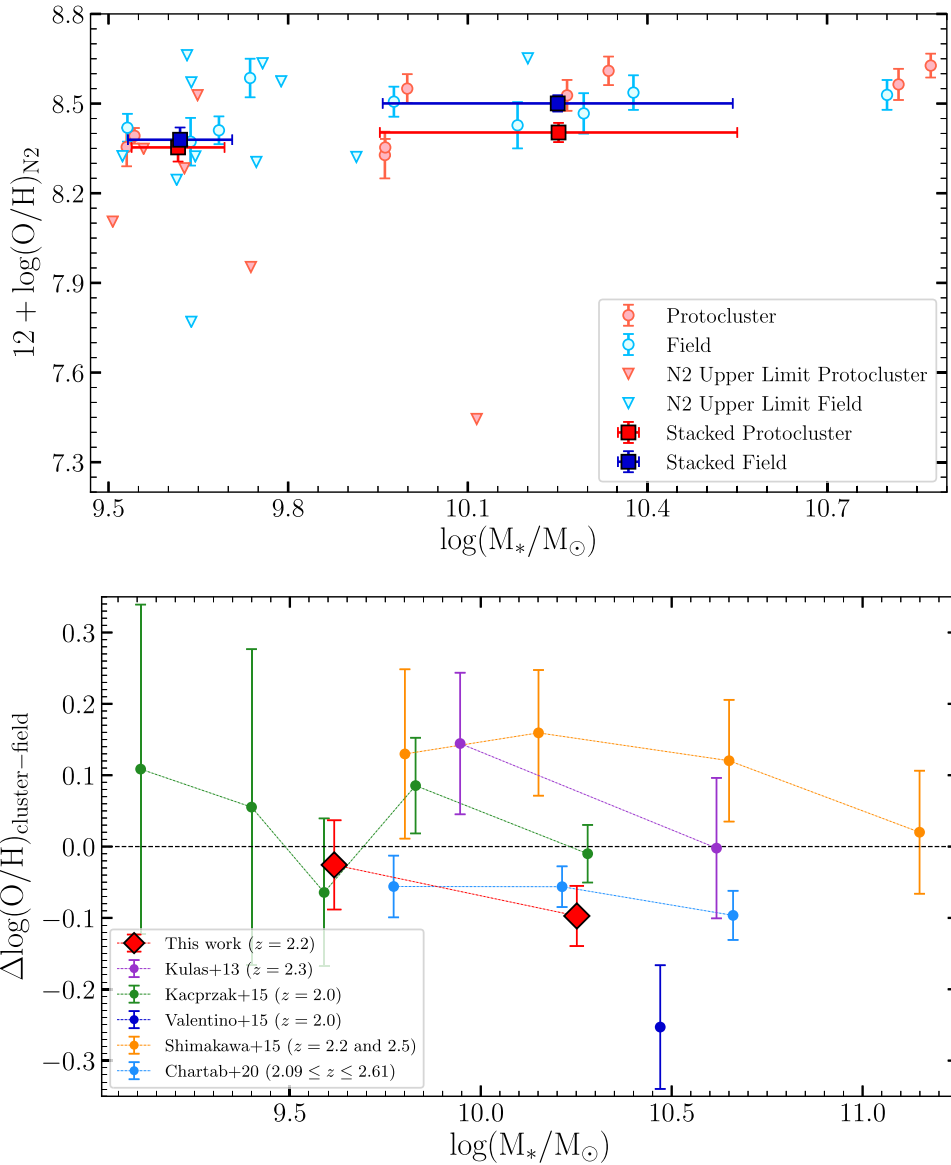
Figure 5. Top: the MZR for the mass-matched samples at $z \sim 2.2$ for protocluster galaxies (red) and field galaxies (blue). Inverted triangles show [N ii]$\lambda6584$ nondetections. The gas-phase metallicities for stacked spectra of protocluster and field samples in two stellar mass bins of $10^{9.5} \, M_\odot \leqslant M_* < 10^{9.9} \, M_\odot$ and $10^{9.9} \, M_\odot \leqslant M_* \leqslant 10^{10.9} \, M_\odot$ are also shown in red and blue squares, respectively. The horizontal error bars in the stacked data show 1σ scatter in stellar mass of each bin. Bottom: the compilation of the difference (offset) between gas-phase metallicity of protocluster and field galaxies as a function of stellar mass from literature. The red data points show the offset for the mass-matched samples used in this work in two stellar mass bins. The uncertainties in the offsets include errors from gas-phase metallicities of both protocluster and field samples.

metallicity. This metal enhancement at lower redshifts in dense environments compared to field galaxies is observed in previous studies (e.g., Cooper et al. 2008; Ellison et al. 2009; Darvish et al. 2015).

ORCID iDs

Zahra Sattari ⬡ https://orcid.org/0000-0002-0364-1159
Nima Chartab ⬡ https://orcid.org/0000-0003-3691-937X
Behnam Darvish ⬡ https://orcid.org/0000-0003-4919-9017
Irene Shivaei ⬡ https://orcid.org/0000-0003-4702-7561
Nick Scoville ⬡ https://orcid.org/0000-0002-0438-3323
David Sobral ⬡ https://orcid.org/0000-0001-8823-4845

References

Alcorn, L. Y., Gupta, A., Tran, K.-V., et al. 2019, ApJ, 883, 153

Balogh, M., Eke, V., Miller, C., et al. 2004, MNRAS, 348, 1355
Behroozi, P. S., Wechsler, R. H., & Conroy, C. 2013a, ApJL, 762, L31
Behroozi, P. S., Wechsler, R. H., & Conroy, C. 2013b, ApJ, 770, 57
Bruzual, G., & Charlot, S. 2003, MNRAS, 344, 1000
Byler, N., Dalcanton, J. J., Conroy, C., & Johnson, B. D. 2017, ApJ, 840, 44
Calzetti, D., Armus, L., Bohlin, R. C., et al. 2000, ApJ, 533, 682
Carnall, A. C., McLure, R. J., Dunlop, J. S., & Davé, R. 2018, MNRAS, 480, 4379
Chabrier, G. 2003, PASP, 115, 763
Chartab, N., Mobasher, B., Darvish, B., et al. 2020, ApJ, 890, 7
Chartab, N., Mobasher, B., Shapley, A. E., et al. 2021, ApJ, 908, 120
Coil, A. L., Aird, J., Reddy, N., et al. 2015, ApJ, 801, 35
Cooper, M. C., Newman, J. A., Weiner, B. J., et al. 2008, MNRAS, 383, 1058
Darvish, B., Mobasher, B., Sobral, D., et al. 2015, ApJ, 814, 84
Darvish, B., Mobasher, B., Sobral, D., et al. 2016, ApJ, 825, 113
Darvish, B., Scoville, N. Z., Martin, C., et al. 2020, ApJ, 892, 8
Dekel, A., & Birnboim, Y. 2006, MNRAS, 368, 2
Dekel, A., Birnboim, Y., Engel, G., et al. 2009, Natur, 457, 451
Donley, J. L., Koekemoer, A. M., Brusa, M., et al. 2012, ApJ, 748, 142
Dressler, A. 1980, ApJ, 236, 351
Duncan, K., Conselice, C. J., Mundy, C., et al. 2019, ApJ, 876, 110
Ellison, S. L., Simard, L., Cowan, N. B., et al. 2009, MNRAS, 396, 1257
Erb, D. K., Shapley, A. E., Pettini, M., et al. 2006, ApJ, 644, 813
Garn, T., & Best, P. N. 2010, MNRAS, 409, 421
Geach, J. E., Sobral, D., Hickox, R. C., et al. 2012, MNRAS, 426, 679
Hine, N. K., Geach, J. E., Alexander, D. M., et al. 2016, MNRAS, 455, 2363
Horne, K. 1986, PASP, 98, 609
Horstman, K., Shapley, A. E., Sanders, R. L., et al. 2021, MNRAS, 501, 137
Kacprzak, G. G., Yuan, T., Nanayakkara, T., et al. 2015, ApJL, 802, L26
Kauffmann, G., White, S. D. M., Heckman, T. M., et al. 2004, MNRAS, 353, 713

Kawinwanichakij, L., Papovich, C., Quadri, R. F., et al. 2017, ApJ, 847, 134
Kennicutt, Robert C., Jr. 1998, ARA&A, 36, 189
Kereš, D., Katz, N., Weinberg, D. H., & Davé, R. 2005, MNRAS, 363, 2
Koyama, Y., Smail, I., Kurk, J., et al. 2013, MNRAS, 434, 423
Kriek, M., Shapley, A. E., Reddy, N. A., et al. 2015, ApJS, 218, 15
Kulas, K. R., McLean, I. S., Shapley, A. E., et al. 2013, ApJ, 774, 130
Laigle, C., McCracken, H. J., Ilbert, O., et al. 2016, ApJS, 224, 24
Lara-López, M. A., Cepa, J., Bongiovanni, A., et al. 2010, A&A, 521, L53
Maiolino, R., & Mannucci, F. 2019, A&ARv, 27, 3
Mannucci, F., Cresci, G., Maiolino, R., Marconi, A., & Gnerucci, A. 2010, MNRAS, 408, 2115
McLean, I. S., Steidel, C. C., Epps, H. W., et al. 2012, Proc. SPIE, 8446, 84460J
Mehta, V., Scarlata, C., Capak, P., et al. 2018, ApJS, 235, 36
Peng, Y.-j., Lilly, S. J., Kovač, K., et al. 2010, ApJ, 721, 193
Peng, Y.-j., & Maiolino, R. 2014, MNRAS, 438, 262
Pettini, M., & Pagel, B. E. J. 2004, MNRAS, 348, L59
Sanders, R. L., Shapley, A. E., Kriek, M., et al. 2018, ApJ, 858, 99
Scoville, N., Aussel, H., Brusa, M., et al. 2007, ApJS, 172, 1
Shapley, A. E., Sanders, R. L., Shao, P., et al. 2019, ApJL, 881, L35
Shimakawa, R., Kodama, T., & Tadaki, K. i. 2015, MNRAS, 448, 666
Sobral, D., Best, P. N., Matsuda, Y., et al. 2012, MNRAS, 420, 1926
Sobral, D., Best, P. N., Smail, I., et al. 2014, MNRAS, 437, 3516
Sobral, D., Smail, I., Best, P. N., et al. 2013, MNRAS, 428, 1128
Sobral, D., Stroe, A., Dawson, W. A., et al. 2015, MNRAS, 450, 630
Steidel, C. C., Rudie, G. C., Strom, A. L., et al. 2014, ApJ, 795, 165
Stott, J. P., Sobral, D., Bower, R., et al. 2013, MNRAS, 436, 1130
Valentino, F., Daddi, E., Strazzullo, V., et al. 2015, ApJ, 801, 132
Watson, C., Tran, K.-V., Tomczak, A., et al. 2019, ApJ, 874, 63